Experimental Investigation of Aerosol Deposition in Alveolar Lung Airways

Raf Theunissen[1], Nicolas Buchmann[1], Patricia Corieri[1], Michel L. Riethmuller[1], Chantal Darquenne[2]

1: von Karman Institute for Fluid Dynamics, Rhode-Saint-Genèse, Belgium, raf.theunissen@vki.ac.be
2: University of California-San Diego, Department of Medicine, San Diego, USA, cdarquenne@ucsd.edu

Abstract Studies related to aerosol deposition in the alveolar pulmonary airways have been mostly restricted to numerical studies, which require further experimental validation. Few experimental studies have been performed extracting quantitative data due to the involved complexity accompanying the extremely low Reynolds-numbers (in the order of 0.01) encountered in the lower lung airways. This article presents measurements of both fluid velocity and aerosol trajectories conducted in a curved pipe with cylindrical cavities representing the alveolar structures in the 21st generation in the Weibel model. These could later be used in the validation of numerical codes. It turned out to be impossible to model simultaneously Reynolds, gravitational and inertial similarity for the aerosol particles. As one of the main objectives was to act as a benchmark test for numerical codes rather than to accurately simulate the conditions encountered in the alveoli, iron particles of 1.2mm in diameter were chosen for, representing aerosols with in-vivo diameters of 12.8μm. Silicone oil served as carrier fluid allowing flow rates of 0.84ml/s corresponding to Reynolds numbers of 0.07. Using iron particles of 20μm as tracers, PIV experiments were conducted to extract the steady flow velocity distributions. After background subtraction the images were processed with an algorithm, which combines the advantages of multigrid window distortion during the iterative interrogation process and ensemble correlation. As such the negative influences of poor image quality and low seeding could be lessened. A time-resolved tracking algorithm was developed to extract the particle positions from the digitally recorded images. A curvilinear separation streamline at the alveolar openings characterized the flow field and indicated little convective change with the lumen flow. Tubular vortices were found in the corners of the outer radius of the bend which then merged into a larger vortex when reaching the inner radius. The velocity inside the alveoli was about two orders of magnitude smaller compared to the mean lumen velocity. Through the advanced interrogation methodology, allowing correlation windows of 20×20 pixels, even slow rotating fluid elements located at the center of each cavity could be properly identified. None of the injected aerosols were able to follow the tube geometry perfectly. All aerosol trajectories showed a curvilinear behavior indicating gravity as the dominating deposition mechanism. The Stokes number along the particle trajectories was in the order of 10^{-4} proving viscous forces to overrule the inertial forces.

1. Introduction

Aerosol particles are increasingly recognized either as possible health risks in the environment or as diagnostic and therapeutic tool in medical research. Particularly, small particles, which reach the gas-exchange surfaces of the alveolar region of the lung, are considered as potential health risks. The use of inhalers for example has become a common method of drug delivery (Dunbar and Hickey, 2001). Besides serving as systematic treatment, aerosols can also be used in the diagnosis, prevention or control of lung diseases. Pulmonary drug delivery has the advantage that it can deliver drugs directly to the region of therapeutic treatment, hence requiring lower medicine doses. Due to the poor spatial targeting, the therapies aiming at delivering aerosolized drugs directly to the region of interest suffer however from a lower efficiency and possible side effects. Thus the knowledge of spatial targeting requires the knowledge of the nature of the aerosol being delivered and its behavior in the lung. Studies related to aerosol deposition in the alveolar pulmonary airways have been mostly restricted to numerical studies, which require further experimental validation.

Lungs are a network of bifurcations and divided into generations, as modeled by theWeibel morphology (Weibel, 1963). The higher the generation number the deeper down inside the lung the particular region can be found. The higher generation numbers, i.e. larger than 17, represent the alveolar region in which flow velocities in the order of 1cm/s are encountered (Re«1), i.e. Stokes flow. An extensive literature can be found on the numerical simulation of the bifurcations under Stokes conditions (e.g. Crowder *et al.*, 2002). Several research groups have developed realistic two- and three-dimensional computer models of the alveolar region based on Weibel's morphological data (Darquenne 2001, 2002; Darquenne *et al.* 1997, Darquenne and Paiva 1996). They showed the discrepancy in aerosol deposition per airway generation between a rhythmically moving alveolar model and that found in the classical rigid wall model. Based on a mathematical model of a single alveolus, Haber and Tsuda (1998) and Leeming and Schroter (2003) came to the same conclusion. Numerical models now have to take all above-mentioned effects into account to retrieve a valuable simulation, drastically increasing their complexity. Little work has been done however to experimentally validate calculated particle trajectories in the pulmonary acinus due to the required complexity of the setup.

Due to the complexity accompanying the extremely low Reynolds-numbers (in the order of 0.01) encountered in the lower lung airways, only few experimental studies have been reported where quantitative data has been extracted. Recently Lee *et al.* (2005) analyzed the respiratory flow dynamics in 18^{th} to 21^{st} airway generation using a Micro-PIV system. They used a rigid model with smooth walls absent of alveolar structures. Tsuda *et al.* (2002) demonstrated through flow visualization studies that chaotic mixing, i.e. stretching and folding (Haber and Tsuda 1998; Tippe and Tsuda 1999; Tsuda *et al*. 1999, 2002; Henry *et al.* 2002) may be key to particle motion within the alveolar lung regions. Karl *et al.* (2004) and Tippe *et al*. (1999) investigated viscous flow through ducts with moving and rigid cavities of different aspect ratios and showed that the flow is extremely sensitive to the alveolar geometry. All conducted in vitro experiments mentioned above did either not take into account the physical, i.e. non-ideal tracer behavior of the aerosols, but were focused on the reigning flow velocity distribution or were limited to only one alveolus. Theunissen *et al.* (2004) examined experimentally particle trajectories in low Reynolds number flows (Re≈2.24) using a three-dimensional scaled up model comprising three successive airway generations. However, wall motion and alveolar structures on the wall were not simulated, enabling a validation of calculated particle trajectories rather than a quantitative prediction of aerosol deposition.

This article presents measurements of both fluid velocity and aerosol trajectories conducted in a curved pipe with cylindrical cavities representing the alveolar structures. Serving mainly as a feasibility study and preliminary validation benchmark for numerical calculations, the flow conditions encountered in the 21^{st} airway generation were simulated. The objective of the study presented in this paper was however not to exactly reflect the behavior of the human lung, but to take into account as many essential characteristics of alveolar structures as well as of aerosols.

2. Experimental Model

2.1 Model

The three-dimensional model represented an alveolated bend, which can be seen as a 'half' bifurcation (Fig. 1). The model consisted of two alveolated ducts joint by a non-alveolated bend. Each duct consisted of a cylindrical lumen surrounded by an annulus divided into three alveoli. In total the model featured six toroidal alveoli and a transitional zone. The two ducts were jointed under an angle of 35°, which is half the branching angle between two bifurcating airways (Weibel 1963). The dimensions were roughly scaled up by a factor of 50 to allow in-vitro measurements. As the injected aerosols had to be traced, the model needed to be optically accessible. For this reason a mixture of silicone (base : Silicone Elastomer Sylgard 184, curing agent : Dow Corning USA) was

used as building material. The particularity of the silicon was its transparency and a refractive index equal to that of the carrier fluid (around 1.43). Its high viscosity allowed to match the Reynolds number of 0.07. A lost-model technique was used with a low melting point alloy casted in a mixture of silicone and curing agent. A more elaborate description on the casting procedure of the model can be found in Ramuzat (2002).

The model did not incorporate oscillating wall motion and can be thought of as a simplified model of alveolar ducts that are made of central lumens surrounded by alveolar cavities. Such a model was however acceptable in the context of this study as the main objective was to retrieve information about the influence aerosol characteristics have on their deposition pattern in low Reynolds-number flow conditions.

2.2 Experimental setup

In the simulation, the 21st airway generation was targeted. Silicone oil (ρ=970kg/m³, μ=1Pas) served as carrier fluid allowing, because of its high viscosity, flow rates of 0.84ml/s corresponding to Reynolds numbers of 0.07. The difference in refractive index between model and fluid was negligible reducing optical artifacts and reflections originating from the curved surfaces.

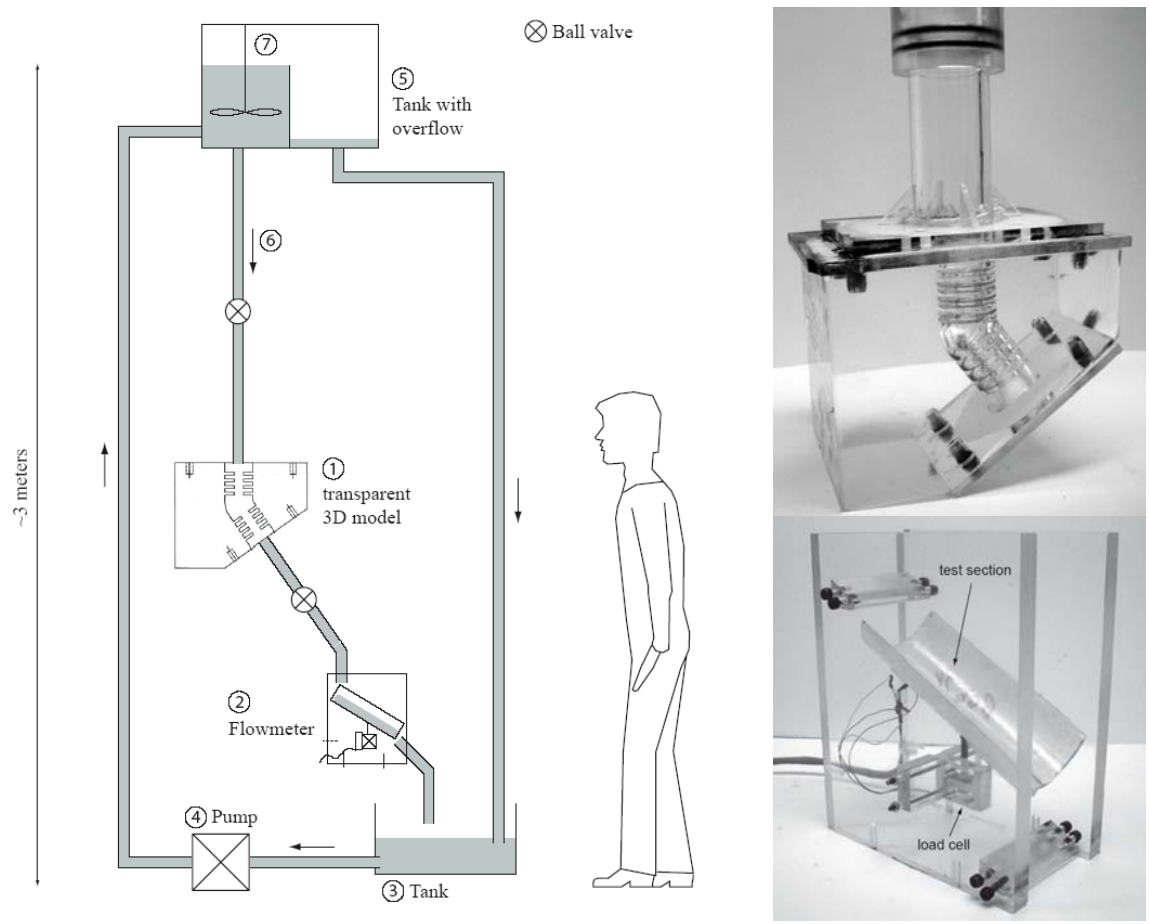

Fig. 1. (Left) Sketch of the experimental setup **(Top Right)** Three-dimensional model of alveolated bend **(Bottom Right)** flow balance developed at VKI

The experimental setup was built on the basis of an existing physiological flow facility at the von Karman Institute and is depicted in Fig. 1. A pump (4) filled the stagnation tank (5), which was connected with a tube (6) leading to the alveolar model (1). After having passed the model the liquid flowed over a flow meter (2) specially designed at the VKI to measure small flow rates. The flow in the model was a gravity flow and the flow rate was regulated by a ball valve downstream.

The liquid dripped into the tank (3) before it was pumped back to the top reservoir. To maintain a constant fluid level, the surplus of fluid in the compartment (5 left) overflowed into a second partition (5 right). The impeller (7) rotated at low speed to keep the fluid in motion such that the added PIV tracer particles would not settle at the bottom of the reservoir. The facility covered a total height of about 3 meters to ensure the required flow rates.

Because of the low flow rates and high viscosity of the used fluids, commercially available flow meters based on inertia driven mechanical systems were not appropriate. A new flow meter developed at the VKI determined the flow rate on the base of the liquid's weight. The essential components are the measurement section and a parallelogram load cell as depicted in Fig. 1. The flow meter was located downstream the model. After passing through the valve the liquid flows over the test section and its weight imposed a force on the load cell underneath. The load cell was equipped with two strain gauges and was enclosed in a four-component Wheatstone bridge. The transducer amplified and translated the signal into voltage, which was related to the flow rate by a preliminary calibration. Given a flow rate of 1ml/s the uncertainty was determined to be about 1.2%.

3. Particle Image Velocimetry

3.1 Processing algorithm

Processing of the images was performed with the cross-correlation algorithm WiDIM, using Fast Fourier Transforms. The algorithm displaced the second exposure interrogation-area with sub-pixel accuracy and optimized it within an iterative structure. The use of sub-pixel accuracy in the displacement allowed higher accuracy. During the iterative procedure, the size of the interrogating windows was gradually reduced (the windows were halved in both directions), yielding a finer resolution in space compared with one step interrogation methods and thereby increasing the spatial resolution. The RMS of the displacement error was thus dramatically reduced to about 10^{-3} pixels. Furthermore the algorithm allowed the use of overlapping windows; instead of having perfectly adjacent windows, their positions overlapped. By letting the windows overlap, the sampling frequency (related to the number of vectors) was increased. More background information on the software can be found in Scarano and Riethmuller (1999).

When evaluating digital PIV recordings with conventional correlation algorithms, a sufficient number of particle images per interrogation window is required to perform a reliable cross-correlation. Typically, an average of four particle images pairs suffice to ensure a reliable and accurate measurement. The current PIV experiments suffered from an insufficient seeding and image quality however within the cavities. Since the flow could be considered as steady due to the low Reynolds number, the present study used a combination of the advanced interrogation method (WiDIM) in combination with an ensemble averaging procedure. The common procedure to enhance the quality of the spatial-average displacement is to average the spatial correlation of corresponding interrogation domains in successive image pairs. If $\phi_k(m, n)$ is the correlation function of a single image pair the average (or ensemble) correlation function for 'N' PIV recording pairs is given by (Wereley *et al.* 2002) as:

$$\phi_{ens}(m,n) = \frac{1}{N}\sum_{k=1}^{N}\phi_k(m,n) \qquad \textbf{(1)}$$

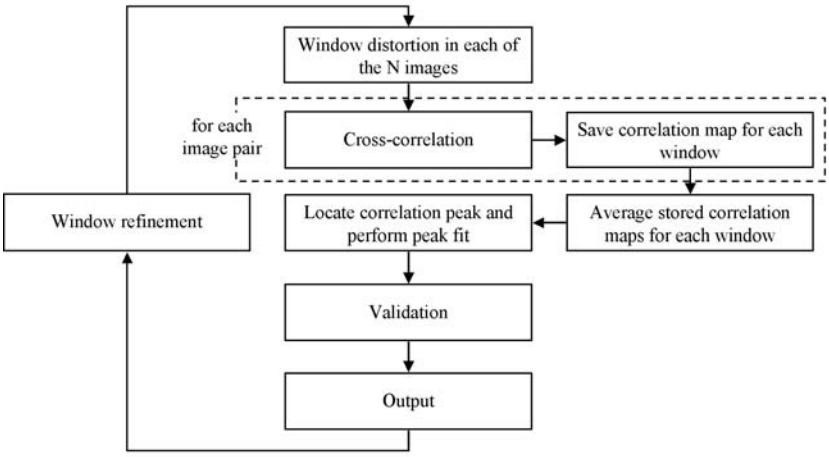

Fig. 2. Combination of ensemble correlation and WiDIM

Fig. 2 depicts the adapted procedure used to process the PIV recordings. This procedure is generally called ensemble correlation or ensemble averaging of spatial correlation estimate and causes the random noise peaks to be significantly reduced through the averaging operation while enhancing the signal peak (Delnoij *et al.* 1999; Meinhart *et al.* 2000) Fig. 3 demonstrates an example of such an averaging process for respectively 2, 20 and 250 PIV images through comparison of the longitudinal and latitudinal profiles of the correlation function.

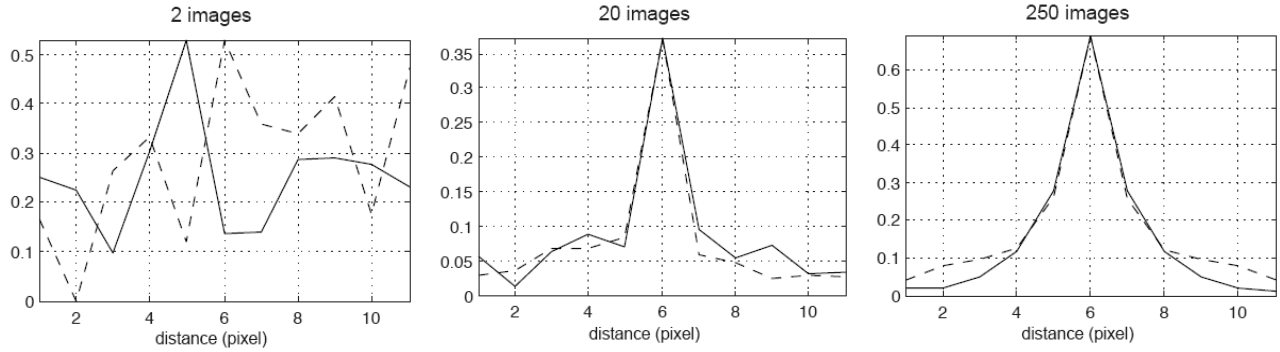

Fig. 3. Evolution of the correlation along the longitudinal (solid) and latitudinal (dashed) symmetry line

3.1 PIV measurement setup

In the performed experiments, the seeding consisted of iron particles of 20µm. They allowed to be mixed with the fluid in a desired quantity and were expected to cause little interferences. Due to their metallic surface they scattered sufficient light providing a clear tracer pattern. The particle relaxation time of $0.17 \cdot 10^{-6}$ seconds allowed the particles to be considered as ideal.

The flow velocities inside the alveolar model were in the order of 10mm/s. The maximal imposed displacement between two consecutive image frames was set to 8 pixels and the magnification was estimated to 0.14. The eight pixels was in agreement with the one-quarter rule proposed by Keane and Adrian (1990), assuming an initial correlation window typically of around 32 pixels in size. The pixel size of the CCD camera was around 10µm, leading to a necessary frame separation time of 57ms or 17.5Hz. The illumination and recording setup is depicted in Fig. 4-a. Relatively large separation times and small flow velocities allowed the use of a continuous illumination source. A continuous Innova 70C Argon laser supplied the coherent light source with a wavelength of 514nm. After passing the laser beam through an optical fiber it was shaped into a thin laser sheet by an optical arrangement. The average sheet thickness was about 1mm, illuminating a slice of the flow located at the symmetry plane. Reflections from the plexiglas

mountings at the top and bottom caused the laser beams to intersect the model several times which resulted in an uneven light intensity distribution inside the test section. To reduce theses interferences the laser sheet was tilted around the horizontal axis and an aperture was placed in front of the model. The scattered light intensities were recorded with a 12bit PCO Sensicam camera, equipped with a 50mm focal length Nikkon lens. An imposed shutter time of 500-1000µs ensured the capture of 'frozen' tracer patterns (Fig. 4-b). The grabbing frequency was imposed by an external trigger, which was connected to a host computer where the camera software was installed. The images themselves had a typical resolution of 1280×640 pixel^2 and an average of 500 images were recorded.

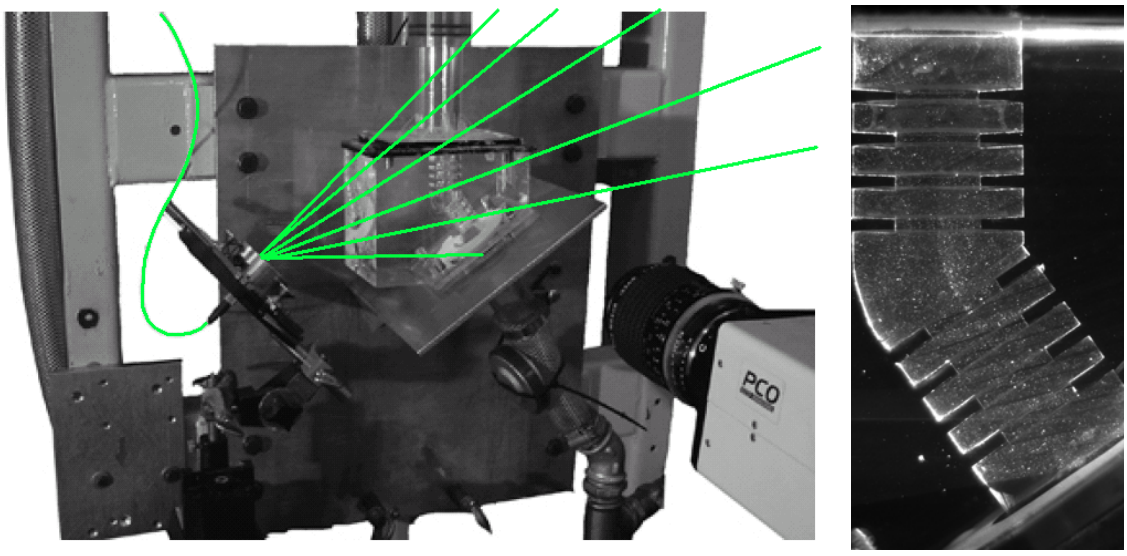

(a) **(b)**

Fig. 4. (a) Image recording setup **(b)** example of an instantaneous PIV recording

4. Time-resolved Particle Tracking Velocimetry

4.1 Principle of Time-tracking

The developed algorithm makes use of reference images (I_0), i.e. recorded images without seeding, to produce a background image. This technique has been proposed by Stitou and Riethmuller (2001). If the instantaneous pixel intensity (I) fulfils the criterion mentioned in equation 2, it is classified as part of a particle. The center of the eventual particle image is determined by a three point Gaussian fit on the intensities in case of a local maximum or by the calculation of the center of gravity of the intensity distribution (Cowen and Monismith 1997).

$$I(i,j) \geq \overline{I_0(x,y)} + 4.2 \cdot RMS[I_0(x,y)] \qquad \textbf{(2)}$$

As no displacement field was available for the particles, the tracking procedure was initialized by the four-frame method proposed by Malik *et al.* (1993). A search area was built around each particle of the first frame (Fig. 5.). All particle images of the second frame located within the area were considered to be possible partners. Based on the assumption that the particles would travel between successive frames the same distance on the same path, search areas in the third and fourth frame were located at the linear extrapolated positions from the two previous frames. Eventually the path with the minimum acceleration was selected from the collection of possible trajectories.

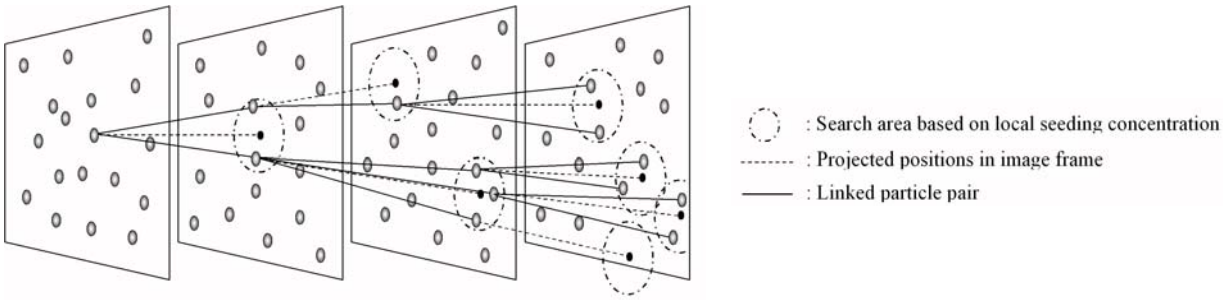

Fig. 5. Principle of the four-frame tracking technique

In case of pairing conflicts, the particle lying closest to the predicted position was considered to be correct. Once a trajectory was established, the participating particles were taken out of consideration in the tracking of the remaining particles. Since numerous trajectories had to be compared, the four-frame method was quite laborious. After the four-frame method, all position predictions were therefore made from a linear extrapolation of the previous particle positions. Again the particle link was performed with the particle located closest to the predicted position. Particle concentrations during the experiments were too low to base the search radius on the detected particle concentration. For this reason a constant value of 20 pixels was imposed and the predicted position did not need to be determined with high accuracy. Displacements of particles were then calculated as the difference between the image centroids. Particle trajectories were validated in that they were limited in the angular deflection in the particle paths. Strongly deviation trajectories created by the four-frame method were in the majority of the cases limited to four time instants. For this reason, paths extending only over 4 frames were removed.

4.3 Aerosol similarity

The equation describing the particle motion under Stokes' conditions assuming the density of the aerosols to be much higher than the carrier fluid is given in dimensionless form by equation 3

$$St\frac{du_p^*}{dt^*} = \left(u_f^* - u_p^*\right) - \frac{u_{pt}}{U}g^* \quad \textbf{where } St = \frac{\rho_p d_p^2 U}{18\mu_f D},\ u_p^* = \frac{u_p}{U}, u_f^* = \frac{u_f}{U},\ t^* = \frac{U}{d_p}t \textbf{ and } g^* = \frac{g}{|g|} \qquad \textbf{(3)}$$

$$u_{pt} = u_p - u_f = \frac{\left(\rho_p - \rho_f\right)\cdot g \cdot d_p^2}{18 \cdot \mu_f} \qquad \textbf{(4)}$$

In equation 3 'U' symbolizes the mean airflow velocity inside the airway with diameter 'D'. Symbols 'ρ_p', 'd_p' and 'μ_f' denote respectively the density of the aerosol particle, it's diameter and the dynamic viscosity of the fluid. 'u_{pt}' is the terminal velocity of the particle relative to the fluid motion (see equation 4). The Stokes number expressing the relative importance of inertial force to viscous force is represented by 'St'. Equation 3 shows that particle motion is governed by two non-dimensional groups; the Stokes' number and the ratio of the particle's terminal velocity to mean fluid velocity.

To simulate aerosol trajectories, particles used under experimental conditions must show a similar behavior as aerosols in the lung. Aerodynamic similarity was ensured by applying the real Reynolds numbers in the model for both the lung flow and aerosols. For similarity in particle deflection caused by gravity and inertia two analogues models were applied to describe their influence; a particle falling vertically under the influence of gravity and a particle in a rotating cylinder with merely inertial forces acting on it. In the latter case the terminal velocity was found when viscous drag balances with centripetal acceleration (mU^2/D).

The modelled aerosols had in vivo diameters of 1μm with a density of 1000kg/m³, leading to a terminal velocity (equation 4) in air (properties : $\mu=1.73 \times 10^{-5}$ Pa s, $\rho=1.229$ kg/m³) of 33μm/s. Based on the diameter the Reynolds number had a value of 2.23×10^{-6}. Satisfying simultaneously both Reynolds similarity and a constant particle-fluid-velocity ratio for the 21st airway generation ($Re\approx0.07$), particles of 56μm in diameter with a density of 20771kg/m³ should have been used. Similarly, keeping the Stokes number constant ($St\approx4.6\cdot10^{-6}$) when the 1μm particle was placed in the rotating cylinder (representing the 21st airway generation), a terminal velocity was reached of about $0.2\cdot10^{-6}$ m/s with a corresponding Reynolds number of $0.01\cdot10^{-6}$. To simulate the aerosol behavior a particle of 56μm in diameter with a density of 850880kg/m³ would be needed.

As none of the two conditions could be satisfied simultaneously it was opted to concentrate only on the imposed velocity ratio between terminal velocity and flow velocity. Spherical iron particles of 1.2mm in diameter were chosen for. Based on the value of the terminal velocity, the equivalent aerosol diameter was 12.8μm. The iron spheres had relaxation times of 624μs. As such it was sure that the particles would not follow the flow streamlines, which can only come to the good of the validation of numerical codes. The choice of iron particles was also made because of their good light scattering ability and their magnetic attraction. The latter was used to handle the particle once they were inside the flow cycle. An electro-magnetic bolt was centered in the symmetry plane of the tube leading to test section. A number of aerosol particles were placed with regularly spacing onto the coil and would remain there under the influence of the magnetic field. Once the experimental flow conditions were adjusted the field was turned off and the particles were released into the flow. Particles that did not deposit inside the model were collected by a permanent magnet downstream the test section to prevent any occlusion of the valves. The magnets are place far enough from the alveolar model such that any interference with the particle trajectories can also be neglected.

5. Experimental results and discussion

5.1 Number of images

The expected measurement error 'ε' in a flow with a certain turbulence intensity ($\sqrt{\overline{u'^2}}/\bar{u}$) is related to the number of images 'n' necessary to pertain a certain confidence level (Bruun, 1995). This relation is given in (5). In the PIV experiments, a total of 500 image pairs were recorded. The RMS over these images proved to be low, as Stokes flow is assumed to be turbulence-free. A relative measurement error in the displacement of 0.88% at a 95% confidence level (CL) was expected, over-assuming a turbulence intensity of 10%.

$$n = \left(\frac{Z_\alpha}{\varepsilon} \frac{\sqrt{\overline{u'^2}}}{\bar{u}} \right)^2 \quad \text{with} \quad CL = erf\left(\frac{Z_\alpha}{\sqrt{2}} \right) \tag{5}$$

5.2 Velocity measurement

Initially interrogation windows of 80×80 pixels² were applied and reduced to final windows of 20×20 pixels² (1.4×1.4 mm²) in three iterations. A window overlap of 50% was imposed in both horizontal and vertical direction, resulting in displacement measurement every 10 pixels. By averaging the correlation-map for each window at each iteration step before continuing the process, the signal-to-noise ratio (defined as the ratio between the highest correlation peak and second highest) could drastically be improved, increasing the reliability of the displacement results.

Fig. 6-a depicts the ensemble averaged contour plot of the total velocity combined with velocity profiles. All profiles have parabolic evolutions, which is in agreement with the theoretical Poiseuille

shape. The maximum velocity appears in the centerline of the lumen tube and equals about 9.55mm/s. Together with a lumen diameter 'D' of about 15mm, the corresponding Reynolds number and flow rate equal 0.069 and 0.84ml/s. These values just slightly differ from the target values of 0.07 and 0.85ml/s.

Two regions of high velocity upstream and downstream of the bend can be identified. When approaching the curved tube the flow decelerates due to the cross-section extension and then again accelerates when it enters the second alveolated duct. The velocity inside the alveoli is about 2 orders of magnitude smaller than the mean lumen velocity and no visible bulk convection between the lumen and the alveoli exists. Within the lumen, parabolic velocity profiles can be seen, indicating a fully developed flow. The profile in the bend is slightly skewed towards the inside wall of the bend and corresponds to that typically found in a curved tube. The skewness originates from the radial acceleration the fluid undergoes when passing through the bend. Due to the small Reynolds numbers encountered the entrance lengths, expressed for laminar flow as $L_e/D=0.06\ Re_D$, are very small, making that this skewness diminishes immediately after reaching the second alveolar duct.

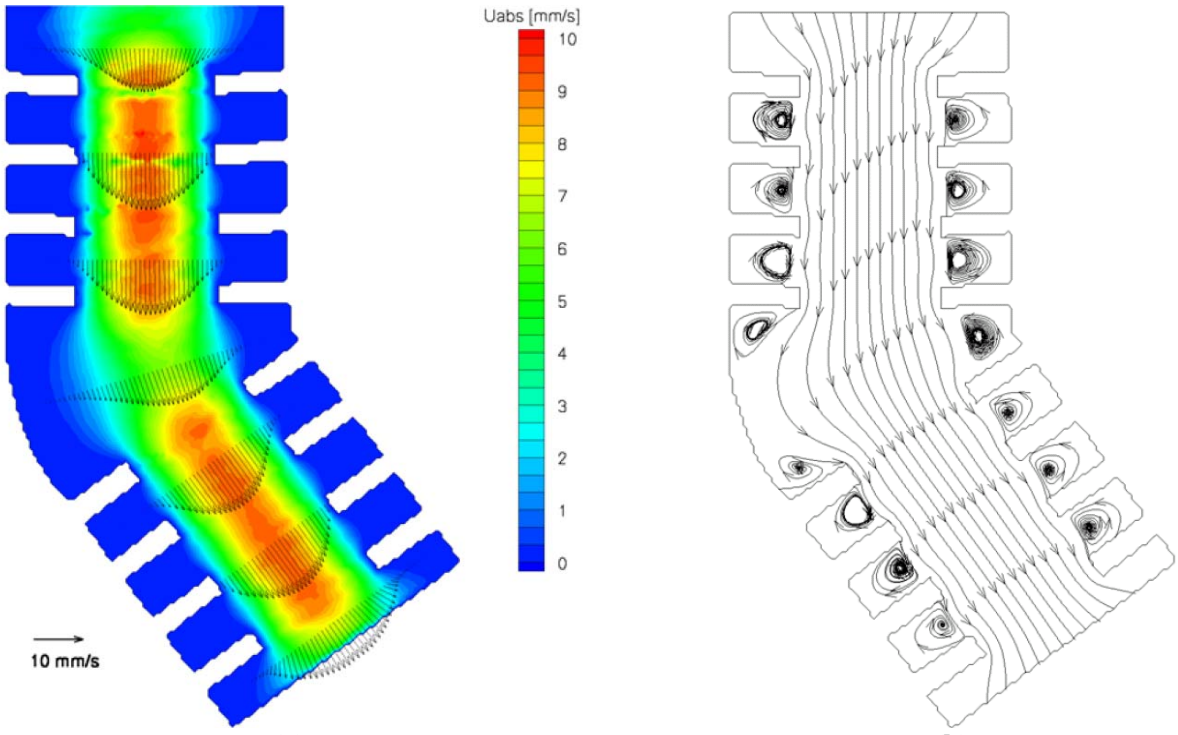

(a) **(b)**

Fig. 6. (a) Total velocity field in the alveolated tube at Re=0.069
(b) Streamline pattern in the tube at Re=0.069

Fig. 6-b illustrates the streamline pattern. The flow field is characterized by curvilinear streamlines at the alveolar openings. A separation streamline at the mouth of the alveolar cavities is present, indicating only little convective exchange between the lumen flow and the surrounding alveoli. Streamlines widen at the bend due to the increase in the cross sectional area and then constrict again when entering the downstream duct. A recirculation flow is positioned inside each alveolus. Tubular vortices are found in the corners of the outer radius of the bend, which then merge into a larger vortex when reaching the inner radius. A close-up of the flow inside the three alveoli on the top right-hand side of Fig. 6-a is displayed in Fig. 7-a. These images were recorded with a larger magnification resulting in a more detailed resolution of the flow field inside the alveolar cavities. The results confirm the formation of a single vortex in the center of the alveolar cavity. Fig. 7-b shows the horizontal and vertical velocity profile superimposed on the contour plot of the

total velocity. Velocities found inside the alveolar cavities are around 0.1mm/s and are approximately two orders of magnitude smaller than the mean lumen velocity. Deep inside the alveoli the flow velocity tends to zero resulting in a stagnation region that roughly covers half the cavity. Both, streamlines and velocity vectors are coherent with results from classical cavity flow theory.

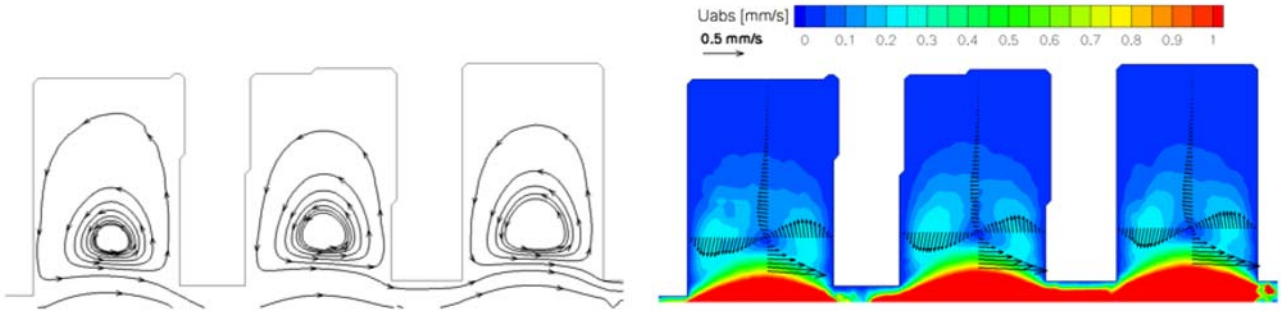

(a) **(b)**

Fig. 7. (a) Streamline pattern in the top right-hand side alveoli Re=0.069
(b) Total velocity field in the top right-hand side alveoli Re=0.069

5.3 Particle Trajectories

Trajectories of particles of 1.2mm were extracted. Having the PIV velocity field available, the particle paths could be compared to those of fluid elements (Fig. 8). None of the particles was capable of following the geometry of the lumen tube. Instead, after passing the entrance of the bend, the trajectories deviated from the flow streamlines. This was due to the influence of the gravity field and the particles inertia. In the upper lumen, where gravity is parallel to the flow direction, the particles followed almost perfectly the flow without visible deviation. As they moved through the bend their paths strongly deviated from streamlines and even crossed them. Especially close to the outer wall, the radius of curvature was too large for the particles to follow. Once the particle entered the lower lumen they moved along a linear pass and were almost mutually parallel. Here they continued to deviate from streamlines and could either enter the lower alveoli or impact the outer lumen wall. All trajectories showed a curvilinear behavior, indicating that gravity was the predominate deposition mechanism. Only particles entering the model at the left side had the possibility to deposit in the alveolar cavities. As the particles moved towards the lumen periphery, the local velocity decreased and forced the particle to decelerate. Particles entering at the inside still deviated from streamlines significantly, but as they moved toward the lumen center their velocity increased.

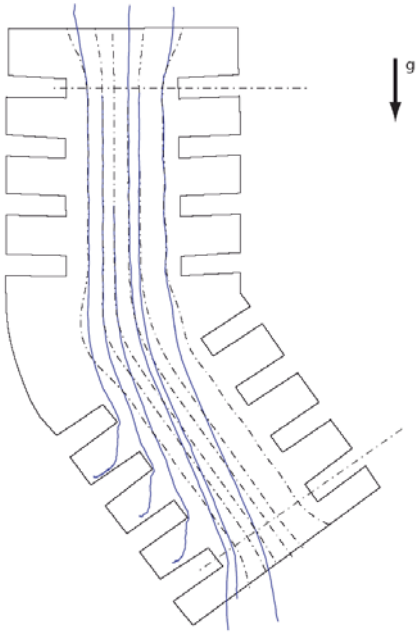

Fig. 8. Comparison between trajectories of iron particles of 1.2mm (solid) and stream lines (dashed)

Having the particle position at each time instant, allowed the calculation of the Reynolds number. The almost constant particle Reynolds number implied that the velocity lag had to be constant and hence also the drag force. Considering only viscous drag and gravitational force (not valid for the bend), may explain the linear trend of the trajectories. Furthermore, the Stokes number was in the order of 10^{-4}, indicating that viscous forces dominated the inertial forces

5. Conclusions

Aerosol particles are increasingly recognized either as possible health risks in the environment or as diagnostic and therapeutic tool in medical research. In particular, small particles, which do not deposit in the airways but reach the gas-exchange surfaces of the alveolar region in the lower pulmonary region, are considered as potential health risks.

In the presented report, an experimental investigation was conducted on the behavior of aerosol particles in the alveolar lung region. The 21st airway generation (Re≈0.07) was modeled by a curved pipe with cylindrical cavities representing the alveolar structures. An initial parameter study was made on to ensure that simulations would be made under realistic conditions. Silicone was used as carrier fluid and iron particles of 1.2mm in diameter represented the aerosols.

An existing cross-correlation algorithm was elaborated to include ensemble correlation. The former incorporates window distortion and reduction of the interrogation windows within an iterative structure. The adapted algorithm allowed the extraction of valuable velocity information with relatively high spatial resolution, even in regions of poor image quality and low seeding. A time tracking algorithm extracted the time-resolved particle positions from digitally recorded images. Incorporated in the algorithm was the four-frame tracking method, followed by a linear extrapolation of previous determined particle locations to serve as predictor for the next position.

A curvilinear separation streamline at the alveolar openings characterized the flow field and indicated little convective change with the lumen flow. In the center of the tube, measured velocity profiles showed good agreement with the theoretical Poiseuille flow. Tubular vortices were found in the corners of the outer radius of the bend which then merged into a larger vortex when reaching the inner radius. The velocity inside the alveoli was about two orders of magnitude smaller compared to the mean lumen velocity. Through the advanced interrogation methodology even the slow rotating fluid elements, located at the center of each cavity could be properly identified . None of the injected aerosols were able to follow the tube geometry perfectly. All aerosol trajectories showed a curvilinear behavior indicating gravity as the dominating deposition mechanism. The Stokes number along the particle trajectories was in the order of 10^{-4} proving viscous forces to overrule the inertial forces.

References

Bruun H.H. (1995), Hot-wire anemometry – principles and signal analysis, *Oxford University press*

Cowen E.A. and Monismith S.G.(1997) A hybrid digital particle tracking velocimetry technique, *Experiments in Fluids*, 22, 199-211

Crowder T.M., Rosati J.A., Schroeter J.D., Hickey A.J., Martonen T.B. (2002) Fundamental effects of Particle Morphology on Lung Delivery: Predictions of Stokes' Law and the Particular Relevance to Dry Powder Inhaler Formulation and Development, *Pharmaceutical Research - Review Article*, Vol.19 No.3

Darquenne C. (2001) A realistic two-dimensional model of aerosol transport and deposition in the alveolar zone of a human lung, *J. of Aerosol Science*, 32, pp.1161-1174

Darquenne C. (2002) Heterogenity of aerosol deposition in a two-dimensional model of human alveolated ducts, *J. of Aerosol Science*, 33, pp.1261-1278

Darquenne C., Brand P., Heyder J., Paiva M. (1997) Aerosol dispersion in human lung : comparision between numerical simulations and experiments for bolus tests, *J. of Applied Physiology*, 83, 3, pp.966-974

Darquenne C., Paiva M. (1996) Two- and three-dimensional simulation of aerosol transport and deposition in alveolar zone of human lung, *J. of Applied Physiology*, 80, 4, pp.1401-1414

Delnoij E., Westerweel J., Deen N.G., Kuipers A.M., van Swaaij W.P.M. (1999) Ensemble correlation PIV applied to bubble plumes rising in a bubble column, *Chemical Engineering*, 54, pp.5159-5171

Dunbar C.A.,Hickey A.J. (2001) Design of aerosol systems for drug delivery to the lungs using numerical methods, *In: Medical applications of computer modeling: the respiratory system*, WIT press Southhampton, Boston

Haber S., Tsuda A. (1998) The effect of flow generated by a rhythmically expanding pulmonary acinus on aerosol dynamics, *J. of Aerosol Science*, 29, 3, pp.309-322

Haber S., Yitzhak D., Tsuda A. (2003) Gravitational deposition in a rhythmically expanding and contracting alveolus, *Journal of Applied Physiology*, 95, 657-671

Karl A., Henry F.S., Tsuda A. (2004) Low Reynolds number viscous flow in an alveolated duct, *ASME*, 126, pp.420-429

Keane R.D., Adrian R.J., Zhang Y. (1995) Super-resolution particle imaging velocimetry, *Measurement Science and Technology*, 6, 754-768

Lee W.J., Kawahashi M., Hirahara H. (2005) Analysis of respiratory flow dynamics in a model of human terminal airway bifurcation using Micro PIV, *Proc. 6th Int. Symp. Particle Image Velocimetry*, Pasadena, California, September 21-23

Leeming A.D., Schroter R.C. (2003) Modeling flow and transport in the alveolar region, *VKI Lecture Series*, 2003-7, von Karman Institute for Fluid Dynamics

Malik N.A., Dracos T., Papantoniou D.A. (1993) Particle Tracking Velocimetry in three-dimensional flows – Part II: Particle tracking, *Experiments in Fluids*, 15, 279-294

Meinhart C.D., Wereley S.T., Santiago J.G. (2000) A PIV algorithm for estimating time-average velocity fields, *J. of Fluids Engineering*, 122

Ramuzat A.(2002) Techniques de mesures non-invasives appliqués aux écoulements biologiques – Etude des bifurcations pulmonaires successives, *PhD Thesis*, von Karman Institute for Fluid Dynamics & Université de Paris XII-Val de Marne

Scarano F. and Riethmuller M.L., Iterative Multigrid approach in PIV image processing with discrete window offset, *Experiments in Fluids* , 26, 513-523, 1999

Stitou A. and Riethmuller M.L. (2001) Extension of PIV to super resolution using PTV, *Measurement Science and Technology*, 12, 1398-1403

Theunissen R., Corieri P., Riethmuller M.L. (2004) Application de la technique PTV à la modélisation d'écoulements d'aérosols dans les voies aériennes pulmonaires, *9ème Congrès Francophone de Vélocimétrie Laser*

Tippe A., Tsuda A. (1999) Recirculating flow in an expanding alveolar model ; experimental evidence of flow-induced mixing of aerosols in the pulmonary acinus, *J. of Aerosol Science*, 31, 8, pp.979-986

Tsuda A., Otani Y., Butler J.P. (1999) Acinar flow irreversibility caused by perturbations in reversible alveolar wall motion, *J. of Applied Physiology*, 86, pp.977-984

Tsuda A., Rick R.A., Hydon P.E., Butler J.P. (2002) Chaotic mixing deep in the lung, *PNAS*, 99, 15, pp.10173-10178

Weibel E.R. (1963) Morphology of the human lung, *Springer Verslag*, Heidelberg

Wereley S.T., Gui L., Meinhart C.D. (2002) Advanced algorithms for microscale particle image velocimetry, *AIAA Journal*, 40, 6